Emergent Materials (2025) 8:7637–7649
https://doi.org/10.1007/s42247-025-01195-5

ORIGINAL ARTICLE

Characterization of size- and shape-controlled magnetic iron oxide microspheres fabricated by the flame method from industrial steel waste

Edison Rivera[1] · Rodrigo A. Muñoz-Meneses[2] · Lorena Marín[3,4] · Malka Mora[5] · Jesús A. Tabares[6] · Luis A. Rodríguez[1,7] · Jesús E. Diosa[1,7] · Ramesh Sivasamy[8] · Edgar Mosquera-Vargas[1,7]

Received: 15 January 2025 / Accepted: 16 July 2025 / Published online: 25 August 2025

Abstract

Magnetic microspheres were fabricated from industrial waste via a single-stage flame spheroidization method using two ferric oxide precursor powders from steel hot rolling industry. The analysis of all samples was carried out by scanning electron microscopy (SEM), X-ray diffraction (XRD), Mössbauer spectroscopy, FTIR and Raman spectroscopy (RS), thermogravimetric analysis (TGA), and vibrating sample magnetometer (VSM). SEM, XRD, Mössbauer spectroscopy, FTIR and RS show the morphology, structure, and phases of the samples studied. The average size for each microsphere was 45 μm (Sample A2) and 60 μm (Sample B2). TGA confirmed the crystallization and phase transition of iron oxides. The VSM study showed high saturation magnetization (M_s) for both microsphere samples, with the higher M_s being very close to the reported value for bulk magnetite and exhibiting a very soft magnetic behavior. The flame spheroidization processing route provides a method for producing microspheres with high uniformity and size control. These factors make the method promising for biomedical, environmental remediation, and energy device applications.

Keywords Industrial waste · Iron oxides · Flame method · Spherical microparticles · Magnetic properties

✉ Rodrigo A. Muñoz-Meneses
ramunoz@unb.br

✉ Edgar Mosquera-Vargas
edgar.mosquera@correounivalle.edu.co

Edison Rivera
edison.rivera@correounivalle.edu.co

Lorena Marín
marin.lorena@correounivalle.edu.co; lmarinm@sgc.gov.co

Malka Mora
malka.mora@correounivalle.edu.co

Jesús A. Tabares
jesus.tabares@correounivalle.edu.co

Luis A. Rodríguez
luis.a.rodriguez@correounivalle.edu.co

Jesús E. Diosa
jesus.diosa@correounivalle.edu.co

Ramesh Sivasamy
rsivasamy@agh.edu.pl

[1] Grupo de Transiciones de Fase y Materiales Funcionales (GTFMF), Departamento de Física, Universidad del Valle, Cali, Colombia

[2] Faculty Gama, University of Brasilia, Gama DF, 72.444-240, Brasília, Brazil

[3] Grupo de Películas Delgadas (GPD), Departamento de Física, Universidad del Valle, Cali, Colombia

[4] Servicio Geológico Colombiano, Dirección de Laboratorios, 111321 Sedes Cali y Bogotá, Colombia

[5] Grupo de Investigación en Síntesis Organometálica y Catálisis (GISIOMCA), Departamento de Química, Universidad del Valle, Cali, Colombia

[6] Grupo de Metalúrgia Física y Teoría de Transiciones de Fase (GMTF) Departamento de Física, Universidad del Valle, Cali, Colombia

[7] Centro de Excelencia en Nuevos Materiales (CENM), Universidad del Valle, Cali, Colombia

[8] Academic Centre for Materials and Nanotechnology, AGH University of Krakow, al. Mickiewicza 30, Kraków 30- 059, Poland

1 Introduction

Pollution is a constantly growing global challenge. Therefore, it is imperative to evaluate this problem and develop solutions to prevent its negative impacts. For instance, the deterioration of water quality leads to an increase in diseases and subsequent loss of life worldwide [1]. The release of sewage and waste into water bodies represents a significant threat to the pollution of lakes and rivers, as well as to the proliferation of garbage and the alteration of natural purification processes of these water bodies in both urban and rural areas. In addition, water contamination with dyes and emerging contaminants originating from various sources such as homes, hospitals, industries, and agriculture, represents a serious health concern, potentially leading to toxicity and diseases like cancer [1, 2]. Hence, employing raw materials and recycling eco-friendly industrial waste at a low cost could serve as a promising alternative to address the challenges associated with water treatment technologies. Furthermore, there is an important need to promote the recycling of industrial waste and facilitate its sustainable development, giving added value to it at a micrometric or nanometric scale employing advanced and environmentally friendly manufacturing techniques.

Because of this environmental problem and the need to reuse industrial recycled materials, in the southwest of Colombia the steel hot rolling industry generates ferric oxide (calamine) with high environmental impact and production costs. Its recycling is only 7% of the amount of steel produced and its commercial use is low compared to the demand of the steel industry [3–5]. Therefore, it is a solid pollutant that is stored in tons, taking up a large space. Recent endeavors have been directed towards reclaiming industrial waste and repurposing it to craft innovative functional materials at either the micrometric or nanometric scale. These efforts aim to introduce fresh advantages to both the environment and society.

Given this, in recent years enormous efforts have been focused on the use of magnetic raw materials for the synthesis and manufacture of micro- and nano-structured iron oxides [6–10]. These iron oxides are significant technologically important due to their physical and magnetic properties. Controlling the synthesis conditions is crucial for achieving the desired structure, as iron oxides exist in various crystalline phases, including magnetite (Fe_3O_4), hematite (α-Fe_2O_3), β-Fe_2O_3, maghemite (γ-Fe_2O_3), ε-Fe_2O_3, and wüstite (FeO). Here, magnetite (Fe_3O_4), hematite (α-Fe_2O_3), and maghemite (γ-Fe_2O_3) are of greatest interest due to their potential range of applications (water treatment, biomedical, hyperthermia, drug delivery, magnetic devices, catalysis, etc.,), abundance, biocompatibility, nontoxicity, and low cost to name some properties [3, 11–22]. Its application arises from the strong magnetism of magnetite (ferromagnetic, $Ms = 92–100$ emu/g at 300 K) and maghemite (ferrimagnetic, $Ms = 60–80$ emu/g at 300 K), which both phases can coexist as a solid solution. While hematite is stable at room temperature, it is weakly ferromagnetic, and its behavior depends on factors such as crystallinity, particle size, and the extent of cation substitution [11]. Literature suggests that the combination of iron oxides and phase transformations can coexist during thermal treatment in the range of 200 °C to 600 °C [8].

The development of fabrication methods of microspheres (MSs) is an ongoing challenge for many researchers. However, glass, polymer, and ceramics MSs and nanospheres (NSs) are commonly manufactured via sol-gel method, spay drying and flame spheroidization processes [23–25]. Spheroidization of powders by flame processing is a technique used to modify the shape of feeding powder particles. This process involves subjecting the powder to a high-temperature flame, causing the particles to melt and form spherical shapes as they solidify. The flame processing method offers several advantages, including the ability to control the particle size and shape, improve flowability, enhance packing density, and reduce porosity. It is commonly used in industries such as metallurgy, ceramics, and powder metallurgy to produce spherical powders for various applications, including additive manufacturing, coatings, and thermal spray.

On the other hand, magnetic MSs are highly used for biomedical applications [23] due to their chemical stability, biocompatibility, and ability to navigate within blood vessels, especially when produced at a size suitable for flowing within hepatic arteries. Magnetite (Fe_3O_4) MSs and NSs have been extensively studied for magnetic-induced hyperthermia treatment of cancers and have demonstrated success as contrast agents in magnetic resonance imaging (MRI) [24]. Moreover, targeted magnetic drug-delivery systems are currently undergoing pre-clinical evaluation. Magnetic MSs have also shown promise in environmental remediation efforts, including the extraction of heavy metals from polluted soil and water, removal of phosphates from wastewater, as well as the absorption of oils, chemicals, and toxins from the environment [1, 24].

Given the potential applications of iron oxides mentioned earlier, we have not found any reports to date regarding the use of iron oxide waste from the steel industry in Colombia as a raw material for producing magnetic iron oxide MSs. The low-cost flame method employed here is ideal due to its features, which enable the successful fabrication of spherical iron oxide powders. This process utilizes irregular iron oxide particles that exchange heat as they pass through the high -temperature region (flame). The particles melt, forming tiny droplets that quickly turn into spheres.

In the flame, the heat cause nucleation and subsequently promotes growth. As the spherical droplets exit the flame and enter a colder region, they rapidly solidify. This study demonstrates, for the first time, a novel application for the use of this industrial waste and a low-cost flame method to produce magnetic iron oxide MSs, which could hold potential applications in areas such as environmental remediation, biomedical, drug-delivery, and devices to name some.

Our focus also includes identifying functional, and cost-effective iron oxide materials as also semiconducting ceramic materials. Therefore, reusing these industrial residues is feasible and can yield novel by-products with increased added value. Furthermore, we have investigated the morphological, structural, and magnetic characteristics of the spherical microparticles (also called microspheres).

2 Experimental section

2.1 Reagents and precursor material

Commercial ethanol (C_2H_5OH, P.A. 96%), acetone (C_3H_6O, P.A. 99.8%), nitric acid (HNO_3, P.A. 65%), ammonium hydroxide (NH_4OH, P.A. 99%) and thinner as solvent were purchased from Sigma-Aldrich, Mallinckrodt Pharmaceuticals and Merck S.A. All reagents are used as supplied without further purification. The raw material employed for the fabrication of microspheres by the flame method originates from industrial waste generated by two steel industry companies located in southwest of Colombia. This waste, see Fig. 1(a-c), comprised mainly of iron oxide, underwent a process of washing and then ground in a ball mill, resulting in particle sizes on the micron scale. The samples received are designated as Sample A and Sample B. Sample B contains industrial rolling process oils as contaminants, posing challenges for the recycling procedure. In addition, a quartering process was carried out on both samples to ensure the acquisition of representative and uniform samples in terms of size and shape. Detailed information on this process can be found in Ref [3]– supporting material, as reported by the authors.

2.2 Sample washing

100 g of each sample underwent a cleaning procedure, involving the addition of this amount to 500 mL of a commercial solvent for 20 min with stirring. After the solvent is removed, the process is repeated again. The samples were subsequently cleaned twice in 400 mL of acetone for 20 min. Following that, the procedure was repeated twice more using 500 mL of ethanol for 10 min each. Subsequently, the excess solvent was removed, and the sample was dried at 60 °C for 24 h. Throughout the process, the washing procedure was maintained with a constant stirring speed of 350 rpm. The sample was ground using a ball mill (ratio 4:1 for 12 h) and sieved (mesh 270) to obtain a fine and homogeneous powder (microparticles, MPs), as seen in Fig. 2**(a)**. The MPs called Sample A1 and Sample B1 were characterized to evaluate the washing process and determine their properties.

2.3 Fabrication of spherical microparticles and sphericity measurements

Following the washing procedure, the iron oxide MSs (here called as Sample A2 and Sample B2) are produced by introducing the cleaned microparticles into the flame reactor, as depicted in Fig. 2(b). The MPs were processed by flame spraying using an oxygen-propane coupled thermal spray gun. After fabrication, magnetic MSs with a particle size of less than 53 μm were gathered and preserved for subsequent characterization. The sieved microparticles and microspheres were placed on an aluminum sample holder using conductive carbon tape to be analyzed by scanning electron microscopy. The samples morphology was analyzed. The sphericity of the observed MSs was determined using Image J software (not shown). Particles at the image peripheries and those overlapping were excluded from quantification.

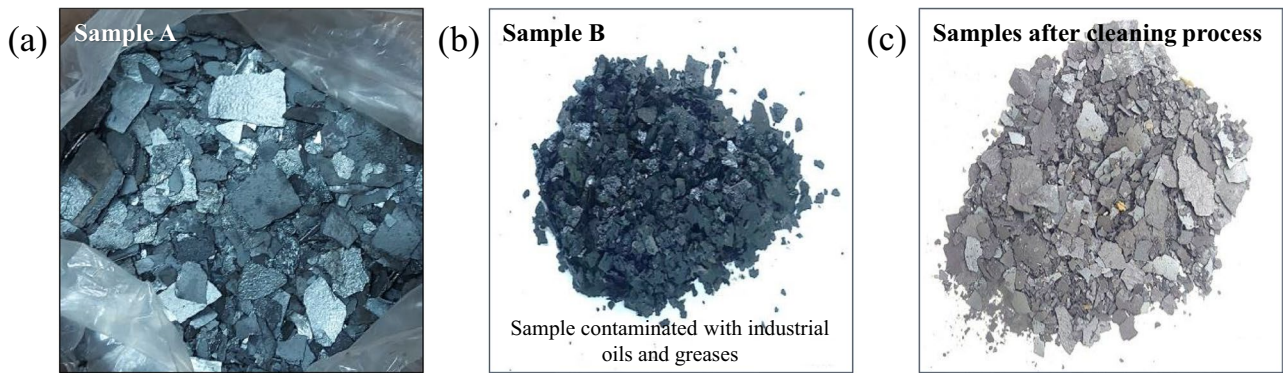

Fig. 1 As received iron oxide lamination (**a**) Sample A, (**b**) Sample B, and (**c**) Samples B after the washing process

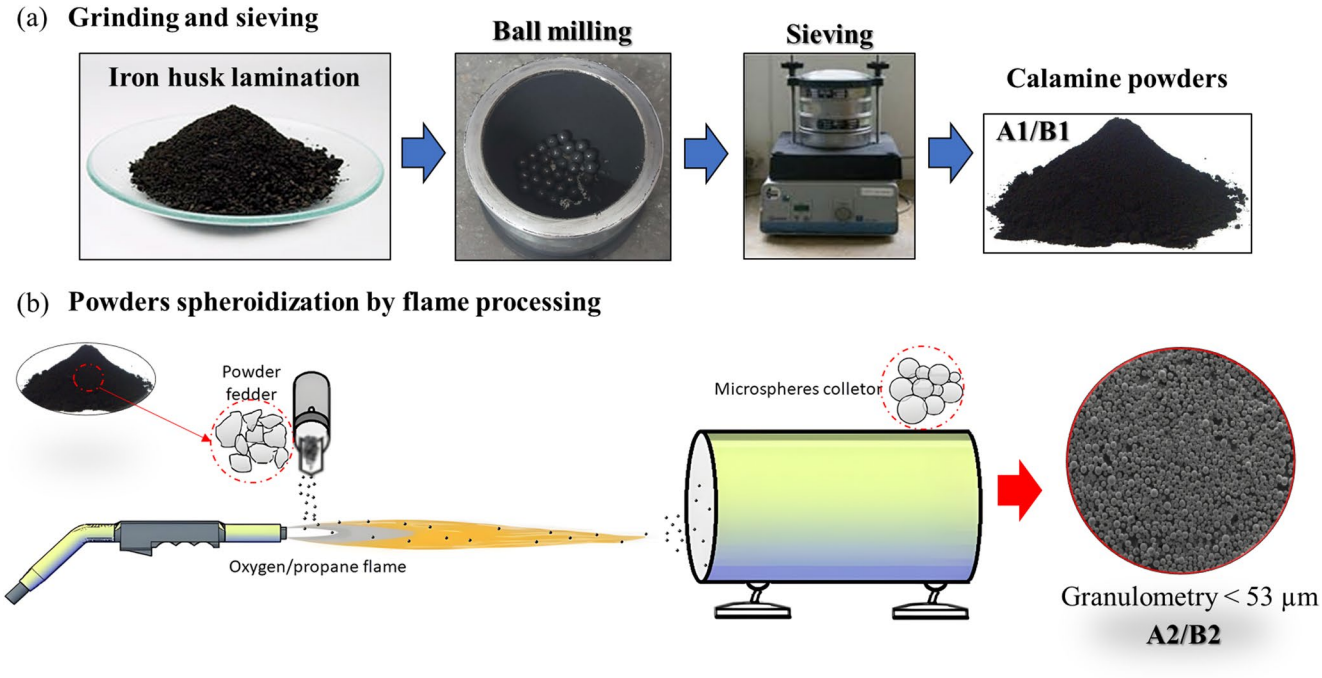

Fig. 2 Schematic representation of the (**a**) grinding and sieving procedure, and (**b**) MS formation via flame processing

2.4 Sample characterization

The morphology and sphericity of the MPs and MSs were obtained using a Phenom Pro X/Scanning electron microscope (SEM). The phases and structure of the samples were analyzed using a PANalytical X´Pert Pro diffractometer in a 2θ angle range of 20–80 degrees (0.01° scan rate, 30 mA, 40 kV). The crystallite sizes (D) of the MSs were calculated by the Debye-Scherrer´s equation, $D = k\lambda/\beta\ cos\theta$, where k is the shape factor (0.95–0.98), λ is the X-ray wavelength (~ 0.154 nm), β is the half-width of the diffraction peak (FWHM) at 2θ, and θ is the Bragg-diffraction angle (peak position) [3, 4, 26]. Mössbauer spectra at room temperature were recorded using a ^{57}Co/Rh radioactive source of ~ 5 mCi. The spectra were fitted with the MOSFIT program [27] and the isomeric shift (IS) were referred to α-Fe. The functional groups present in the MS (prepared as KBr pellets) were determined by infrared spectroscopy, model FTIR 6800 spectrometers from JASCO and using the SPECTRA Manager Analysis software (Version 2). The measurements were recorded at room temperature in the range 4000–350 cm^{-1}. The FTIR spectra obtained were performed at a resolution of 2 cm^{-1}. The Raman spectra were acquired using a confocal micro-Raman spectrometer, model NRS-4500 from Jasco, and diode laser with excitation wavelength of 785 nm. Here, the fluorescence processes are minimized with the line at 785 nm and the laser spot size was 1 µm. However, this small laser spot size produces higher energy, potentially causing changes in the samples. These changes could manifest as a shift or broadening of vibrational bands, or strong disturbance in the Raman fingerprint [28]. To prevent sample modification during Raman measurements, the laser power was adjusted to 2.7 mW for the experiments. A Thermogravimetry-differential thermal analysis (TG-DTA, TA Instrument) was used to determine the temperatures in the thermal transition of the MSs, while a nitrogen (N_2) gas flow was used at a heating rate of 10 °C/min from room temperature to 1300 °C for the analysis. This configuration should allow accurate measurements of the thermal behavior of the microspheres within the specified temperature range. The field dependent magnetization (M-H curves) of MSs was measured at room temperature using a superconducting quantum interference device (SQUID) with a Magnetic Property Measurement System XL from Quantum Design Inc. M-H curves were performed employing a maximum applied field of 20 kOe in either direction.

3 Results and discussion

3.1 Analysis of precursor Raw materials (Sample A1 and sample B1)

3.1.1 Morphological, phase and structural studies

Figure 3 shows the morphological and structural study of Sample A1 and Sample B1 after the washing process. The morphological study of each sample reveals a granulometry

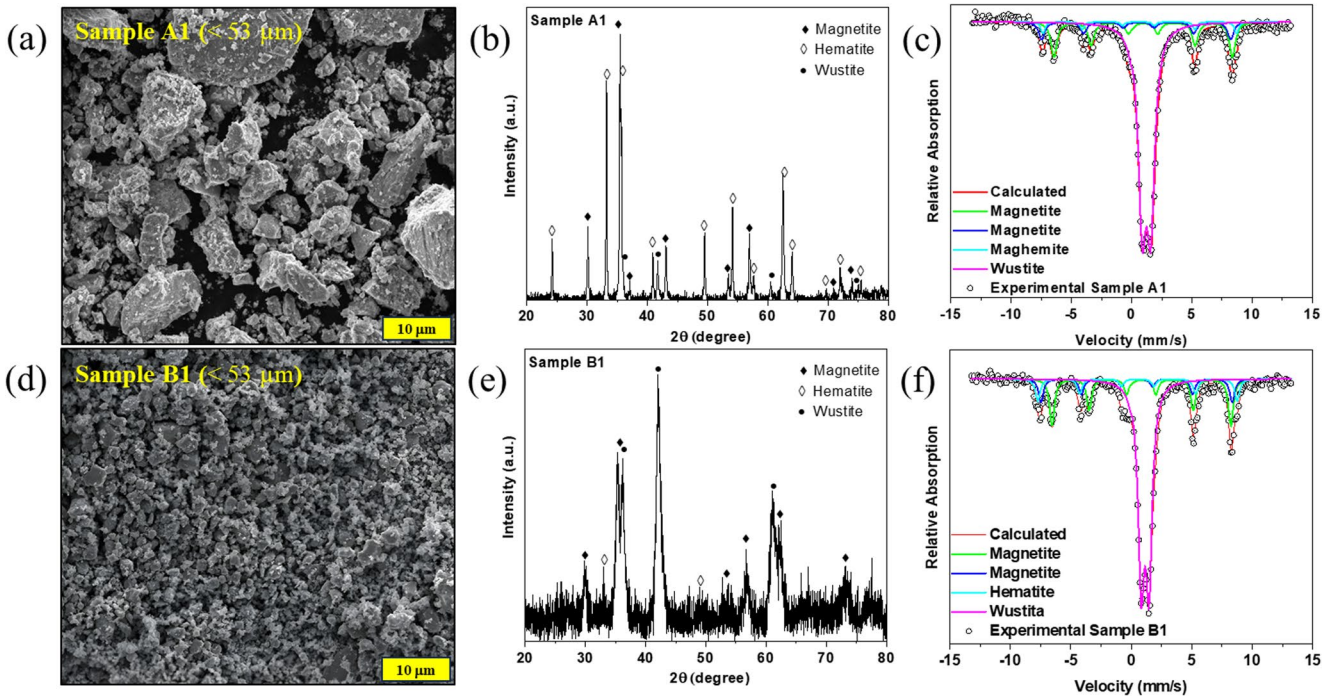

Fig. 3 SEM, XRD, and Mössbauer analysis of the precursor raw materials. (**a-c**) Sample A1 and (**d-f**) Sample B1. The experimental data in the Mössbauer analysis is presented as open circles and the calculated fit as a line

Table 1 Mössbauer parameters of fitted spectra of all the samples. Isomeric shift (IS), quadrupole shift (QS), hyperfine magnetic field (BHF), and relative area (RA) of the line

Sample	IS (mm/s)	QS (mm/s)	BHF (kOe)	RA (%)	Phase
Sample A1	0.305	0.009	492	9.7	Magnetite *A* site
	0.779	0.003	456	19.4	Magnetite *B* site
	0.448	0.531	497	4.4	Maghemite
	1.006	0.709	0	66.5	Wüstite
Sample B1	0.279	−0.041	488	10.8	Magnetite *A* site
	0.653	0.017	456	21.7	Magnetite *B* site
	0.344	−0.016	509	10.1	Hematite
	0.918	0.641	0	57.4	Wüstite
Sample A2	0.316	−0.136	484	20.8	Magnetite *A* site
	0.633	−0.049	457	41.6	Magnetite *B* site
	0.293	−0.015	496	34.7	Maghemite
	0.630	2.351	0	2.9	Fe^{2+}
Sample B2	0.331	−0.176	482	19.9	Magnetite *A* site
	0.665	−0.046	453	39.7	Magnetite *B* site
	286	−0.011	492	37.4	Maghemite
	0.608	2.340	0	3.0	Fe^{2+}

of less than 53 µm. Nevertheless, it was observed that Sample A1 exhibits irregular morphology compared to Sample B1 which is more homogeneous, as shown in Figs. 3(a) and 3(d). In addition, for both samples the XRD patterns was carried out to determine the structure and phases presents. Here, it was observed that three mixed phases of iron oxides coexist, which correspond to magnetite (Fe_3O_4, ICOD 01-076-1849/ICOD 01-088-0315), hematite (α-Fe_2O_3, ICOD 01-087-116/ICOD 01-084-0307) and wüstite (FeO, ICOD 00-001-1223/ICOD 01-84-0302), respectively (see Figs. 3(b) and 3(e)). The structure of the samples was determined using the X´Pert HighScore Plus software (V3.0, database code 2021) provided by Malvern Panalytical. In addition, room-temperature Mössbauer spectra were conducted to confirm the phases present in the XRD for both samples, see Figs. 3(c) and 3(f). The spectra of the samples were fitted with three sextets and one doublet. Two of the sextets are attributed to the magnetite (Fe_3O_4) phase, one corresponding to tetrahedral sites (A site; Fe^{3+}) and the other to octahedral sites (B site; Fe^{3+} and Fe^{2+}) [29]. Another sextet was associated with the Fe^{3+} ions in hematite (α-Fe_2O_3, Sample B1), and with the Fe^{3+} ions in maghemite (γ-Fe_2O_3, Sample A1). For both samples, there is a doublet that can be attributed to a non-stoichiometric wüstite (FeO) phase [30]. The results are summarized in Table 1. After analyzing the composition, structure of the precursor materials A1 and A2, our focus has now shifted solely to investigating the final synthesized microspheres, A2 and B2.

3.2 Analysis of microspheres materials (Sample A2 and sample B2)

3.2.1 Morphological, phase and structural analysis

Unlike the samples A1 and B1, the synthesized microspheres A2 and B2 exhibit a homogeneous morphology. Figures 4(a)–(f) show the typical SEM images of the synthesized samples. The samples exhibit the formation of MSs with average sizes around 45 µm (Sample A2) and 60 µm (Sample B2), as shown in Figs. 4(b), (c), (e) and (f), and histogram inset. Furthermore, in Figs. 4(c), (e), and (f) MSs with superficial porosity, hollow, and with evident grains with heterogeneous sizes can be observed. For each sample, the average size distributions of the microspheres were determined by measuring the diameter of 400 particles, ensuring a measurement confidence greater than 95%.

On the other hand, Figs. 5(g) and (h) show the XRD patterns of the fabricated MSs, which were analyzed the crystal structure and confirmed the presence of the magnetite, maghemite, or both mixed iron oxides similar to their precursor materials. However, complementary analyses are required to determine the phases present because the magnetite and maghemite present similar crystal structures and lattice parameters. Furthermore, the results indicate that both samples exhibit a magnetite structure. The patterns are in good agreement with previously reported data, and no other phases are observed [29, 31]. Given that both crystallize in the same cubic structure, their respective diffracted peaks exhibit similar characteristics, making it challenging to distinguish between these oxides using XRD analysis. Therefore, Mössbauer measurements (vide infra) were carried out to discern between the phases in the samples and corroborate the Raman analysis.

From the X-ray patterns, the average crystallite size of the fabricated microspheres was calculated using Debye-Scherrer equation reported in the sample characterization section. A crystallite size distribution ranging from 40 to 101 nm was observed with an average value of 77.5 and 59.9 nm for Sample A2 and Sample B2, respectively. These results indicates that the MSs are composed with nanocrystals with dimensions on the order of tens of nanometers. Furthermore, it is noted that all XRD peaks exhibit sharpness and intensity, indicative of high crystallinity within the samples.

3.2.2 Mössbauer, FTIR and Raman spectral analysis

Room-temperature Mössbauer spectra of the synthesized MSs are shown in Fig. 4(i) and (j). Each spectrum exhibits a well-developed magnetic hyperfine splitting, which is characteristic of bulk materials. Furthermore, it was noted from the spectral shape that the sample composition does not consist of a single phase. Here, each spectrum is fitted considering three sextets and one doublet. Two of the sextets can be attributed to the magnetite (Fe_3O_4) phase, one corresponding to tetrahedral sites (A site; Fe^{3+}) and the other one is attributed to octahedral sites (B site; Fe^{2+}) [29, 32]. Another sextet is associated to maghemite (γ-Fe_2O_3) phase, while the doublet is attributed to Fe^{2+} ions. The Mössbauer parameters determined from the spectrum fitting are summarized in Table 1. It was also observed for the as-received samples (Sample A1 (Figs. 3(c)) and Sample B1 (Figs. 3(f))) the predominance of wüstite phase, followed by magnetite (Fe_3O_4), and a small presence of hematite (α-Fe_2O_3, 10.1% in Sample B1) and maghemite (γ-Fe_2O_3, 4.4% in Sample A1). Regarding the magnetite (Fe_3O_4) phase, the relative area in all fits indicates that site B has double the area of site A, consistent with stoichiometric magnetite. This adjustment was made to facilitate the accurate identification of the other iron sites in the spectra.

The FTIR spectroscopic analysis of the Sample A2 and Sample B2 revealed significant structural differences in phase distribution and Fe–O bonding interactions, offering valuable insights into the oxidation states and crystalline structures of the iron oxides in both samples (Fig. 5). In the fingerprint region of the spectrum, between 400 and 800 cm^{-1}, characteristic bands were observed, which have previously been linked to Fe–O stretching vibrations in the tetrahedral and octahedral sites of the Fe_3O_4 spinel structure [33, 34]. The presence of these bands in both samples confirms that magnetite is the dominant phase. However, the band at 684 cm^{-1} also suggests a distortion in Fe–O bond symmetry, implying partial transformation into maghemite (γ-Fe_2O_3) [35].

Additionally, the infrared spectra reveal distinct structural differences between Sample A2 and Sample B2, particularly in the Fe–O bonding environment. A well-defined absorption band at 566 cm^{-1} (with a slight shift in sample A2) appears in both spectra, corresponding to Fe–O stretching vibrations in the spinel structure of Fe_3O_4. Furthermore, the 376 cm^{-1} band, consistent with previous studies on magnetite [34], confirms that Fe_3O_4 remains the dominant phase despite varying degrees of oxidation. However, Sample A2 exhibits sharper and more intense bands at 463, 444, and 411 cm^{-1}, characteristic of Fe–O vibrations within an ordered spinel lattice. In contrast, sample B2 shows noticeable attenuation and shifts in these bands, along with the emergence of a new feature at 401 cm^{-1}. This spectral

Fig. 4 (**a**)-(**f**) SEM, (**g**)-(**h**) XRD, and (**i**)-(**j**) Mössbauer analysis for Sample A2 and Sample B2. Inset in (**a**) and (**d**) histograms with the particle size distribution of the MSs. The experimental data in the Mössbauer analysis is presented as open circles and the calculated fit as a line

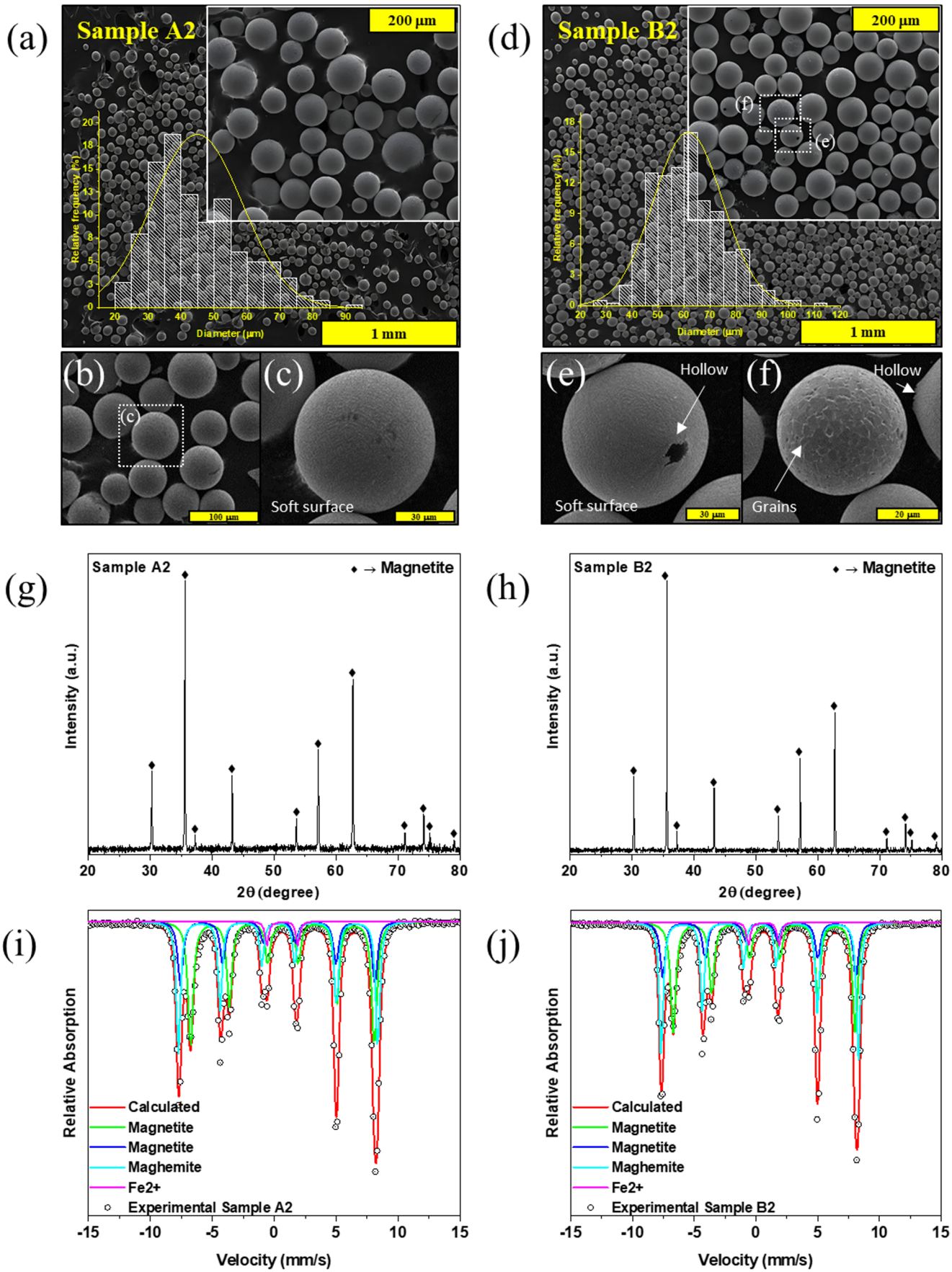
(a)
Sample A2
200 µm
Relative frequency (%)
Diameter (µm)
1 mm
(b)
(c)
100 µm
(c)
Soft surface
30 µm
(d)
Sample B2
200 µm
(f)
(e)
Relative frequency (%)
Diameter (µm)
1 mm
(e)
Hollow
Soft surface
30 µm
(f)
Hollow
Grains
20 µm
(g)
Sample A2
♦ → Magnetite
Intensity (a.u.)
2θ (degree)
(h)
Sample B2
♦ → Magnetite
Intensity (a.u.)
2θ (degree)
(i)
Relative Absorption
Calculated
Magnetite
Magnetite
Maghemite
Fe2+
Experimental Sample A2
Velocity (mm/s)
(j)
Relative Absorption
Calculated
Magnetite
Magnetite
Maghemite
Fe2+
Experimental Sample B2
Velocity (mm/s)

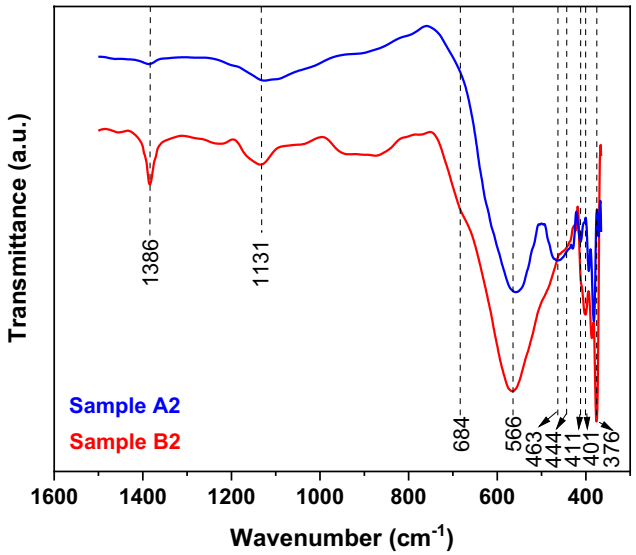

Fig. 5 FTIR spectra of microspheres obtained by flame spheroidization from industrial steel waste

evolution suggests a higher degree of oxidation in sample B2, indicative of a more advanced transformation from Fe_3O_4 to γ-Fe_2O_3, potentially involving intermediate phases [36]. The observed spectral differences between samples A2 and B2 highlight the progressive structural rearrangement of Fe–O bonds during oxidation, which could influence their physicochemical properties and potential applications. Furthermore, bands observed at 1386 cm^{-1} and 1131 cm^{-1}, more prominent in sample B2, may be attributed to the adsorption of functional groups on the microsphere surface. Additionally, the intense absorption band typically associated with the stretching vibration of the O–H group (not shown) is absent in the spectra of both microspheres. This effect can be attributed to the decomposition of the hydroxyl group during the passage of the raw materials through the torch [37, 38].

The Raman spectra of MSs are shown in Fig. 6(a). Raman spectra confirm the structure belonging to magnetite; therefore, two principal vibrational modes are identified in the wavenumber between 200 and 800 cm^{-1}, which correspond to A_{1g} phonon mode at around 674 cm^{-1} (vs.) and E_{1g} phonon mode at 310 cm^{-1} (vw), respectively. However, the vibrational mode associated with the T_{2g} phonon mode was not observed. The different bands of the maghemite structure are not observed. However, it could be said that a weak shoulder (ws) is observed around 710 cm^{-1} and 720 cm^{-1} which could be associated with the maghemite phase (Fig. 6(b) and 6(c)). In addition, a vibrational band at around 1330 cm^{-1} (see inset in Fig. 6(a)) which could be associated with the hematite structure due to the energy from the laser or the fabrication process [39]. In this regard, de Faria et al. [28] previously reported discrepancies in the positions of Raman bands for certain iron oxides and oxyhydroxides, which may closely resemble values expected from the hematite structure. They also noted that the temperature effect induced by laser power could alter the Raman spectrum. Hence, the significant increase in bandwidth they report is attributed to local heating caused by the laser power (ranging from 0.7 to 7 mW), which enhances anharmonic interactions. Moreover, they note that the vibrational mode at approximately 1322 cm^{-1}, attributed to a two-magnon dispersion of hematite, is not a typical feature in a magnetite spectrum but rather a contaminant found in the samples analyzed in prior studies. Consequently, in our scenario, the vibrational mode around 1330 cm^{-1} of hematite could be the result from localized heating induced by the laser (see inset in Fig. 6(a)) [33]. Therefore, the magnetite phase would partly transform into hematite with a laser power of 2.7 mW or higher. However, the experiments performed by de Sousa et al. [28] show that with a laser power less than 2 mW, the samples do not show any change.

Figure 6(b) and 6(c) shows the deconvolution peaks of the A_{1g} phonon mode. For both Sample A2 and Sample B2, the A_{1g} phonon mode associated with the magnetite structure is evident, also appearing as the most intense peak. Moreover, for the Sample A2, two weak bands are observed at 694 and 703 cm^{-1}, while for Sample B2, only the band at 693 cm^{-1} is observed. However, these bands could be assignment to maghemite forming a solid solution with magnetite [11, 29]. Furthermore, for Sample A2, the percentage of magnetite is higher compared to the percentage of maghemite at 703 cm^{-1}. Instead, for Sample B2, the band is imperceptible. These values are very close to those obtained with Mössbauer spectroscopy (see Table 1) assuming that magnetite and maghemite coexist in the MSs.

3.2.3 Thermal stability analysis

Thermal stability of the magnetic MSs, as determined by the TG–DTA analyses, is shown in Fig. 6(d) and (e). The thermograms show that it was possible to observe phase changes when the temperature was raised above 200 and 500 °C. A schematic representation is shown in Fig. 6(f). Here, TG-DTA analysis provides evidence of phase transitions in the iron oxide materials at specific temperatures, confirming that magnetite is stable below 300 °C, can coexist with maghemite below 500 °C, and transforms to hematite above 500 °C. These results confirm the crystallization and phase transition of iron oxides are in agreement with other studies [40], including Raman spectroscopy, and are important for understanding the thermal behavior and stability of magnetic materials.

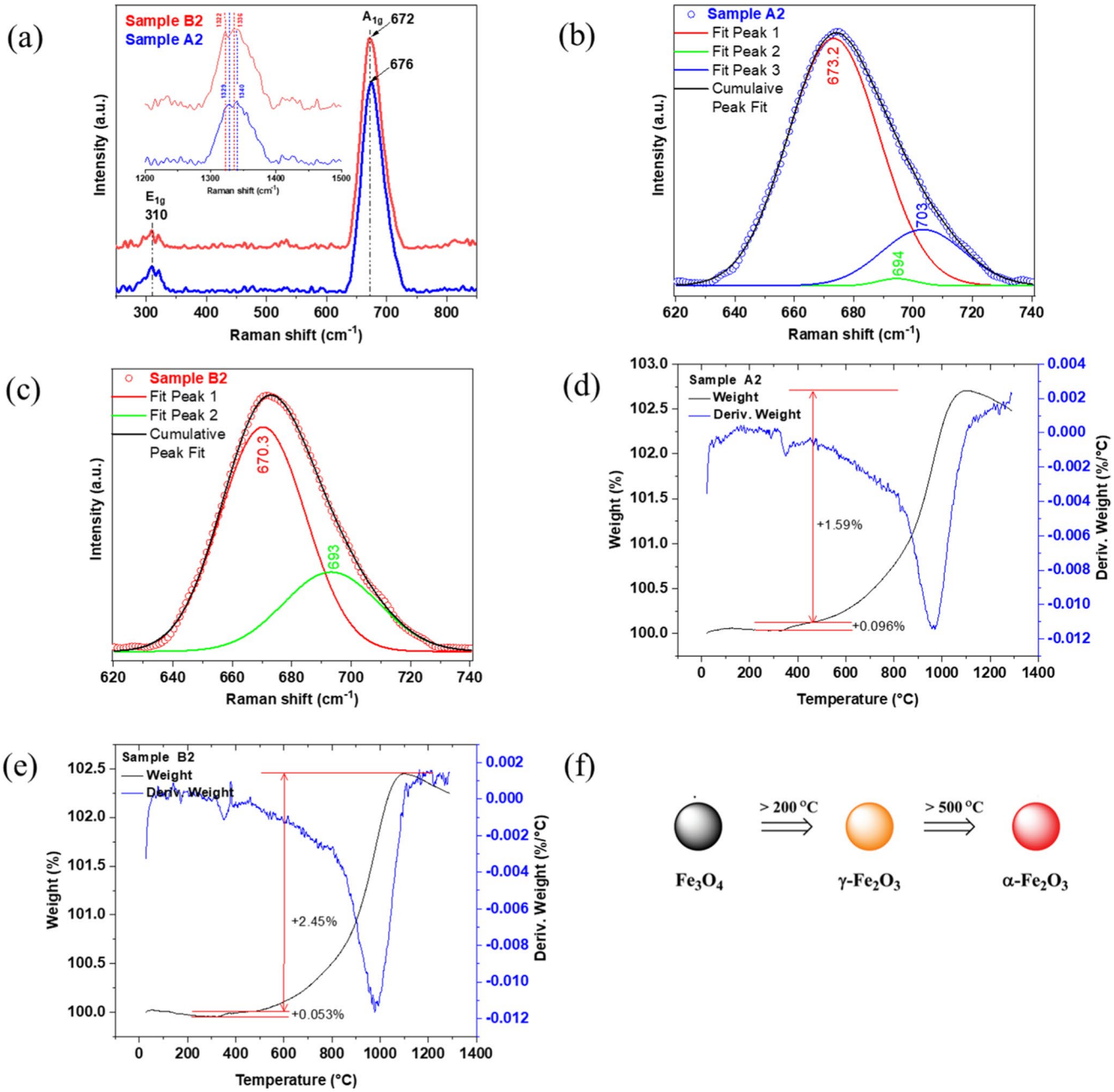

Fig. 6 (**a**) Raman spectra of the MS, (**b**) and (**c**) deconvolutions of the A_{1g} phonon mode, (**d**) and (**e**) thermal analysis for each sample, and (**f**) schematic representation of the phase transformation. Inset in (**a**) peak assigned to a hematite two-magnon scattering

3.2.4 Magnetic studies

Figure 7(a) shows the room-temperature magnetization versus magnetic field (M–H) curves of the synthesized microspheres for both Sample A2 and Sample B2. The hysteresis loop indicates a ferrimagnetic behavior characteristic of the magnetite and maghemite phases [41–43], with high saturation magnetization (M_s) values of 84.81 (Sample A2) and 93.21 emu/g (Sample B2), and very low values of remanent magnetization (M_r) and coercive field (H_c), as shown in Fig. 7(b) and Table 2. Although the Mössbauer analysis do not show significant difference in the relative concentration of magnetite and maghemite between the samples, Sample B2 presents a higher M_s value, which is comparable to that reported for bulk magnetite (typically 92–100 emu/g) [44, 45] and higher than those reported for magnetite nanoparticles [44, 46]. The reduced M_s observed in Sample A2 could arise from several factors, including: (i) overestimation of the effective magnetic mass due to the presence of non-magnetic phases undetected by Mössbauer analysis, (ii)

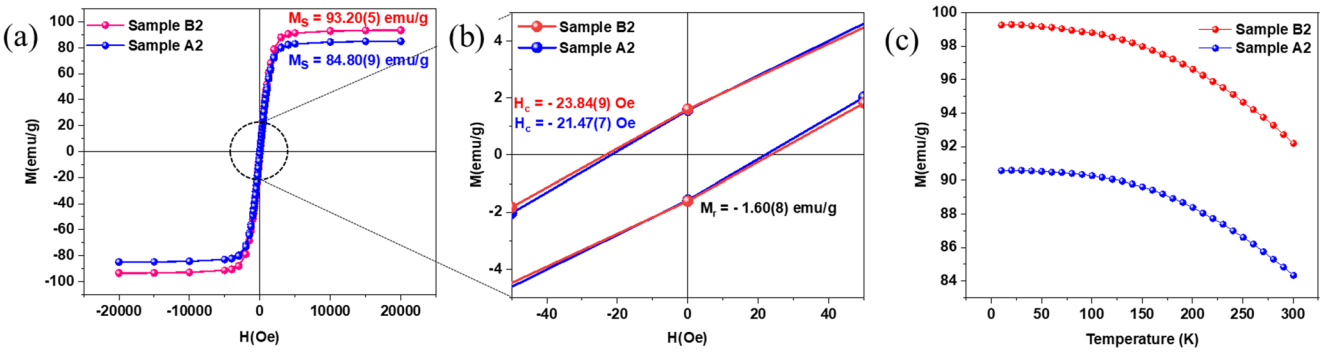

Fig. 7 (**a**) M-H curves for the fabricated MS at RT. A zoom of M-H curves is presented in (**b**). (**c**) FC M-T curves of micro-spheres with increasing temperature

Table 2 Magnetic parameters extracted from M-H curves

Sample	H_c (Oe)	M_r (emu/g)	M_s (emu/g)
Sample A2	−21.47(7)	1.60(8)	84.80(9)
Sample B2	−23.84(9)	1.60(8)	93.20(5)

structural imperfections, (iii) spin canting, or (v) variations in the Fe^{3+}/Fe^{2+} ratio, among others [47, 48].

The very low coercivity and remanence values observed could be attributed to either superparamagnetic or very soft ferrimagnetic behavior. Superparamagnetism typically occurs in magnetite nanoparticles/nanostructures with diameters/crystallite sizes below ~30 nm [44, 46, 48–54]. Although superparamagnetic materials ideally exhibit zero remanence and coercitivity, various experimental studies have shown that magnetite nanoparticles and nanostructures can display values similar to those observed here and still retain superparamagnetic characteristics [46, 54]. However, the crystallite size distribution derived from XRD for our MSs ranges from 40 to 101 nm, which exceeds the typical threshold for superparamagnetic behavior in magnetite and maghemite (~40 nm [51]) nanoparticles. Moreover, very low H_c and M_s values have also been reported in single-crystalline magnetite microparticles (1–40 µm) and thin films [55], which are not superparamagnetic but rather exhibit extremely soft magnetic behavior. Based on these considerations, we conclude that the microspheres synthesized via the flame method exhibit very soft ferrimagnetic characteristics. Soft magnetic materials are generally used in transformers, memory devices, and motors as they reduce energy loss caused by heating during the continuous reversal of the magnetic field in electrical applications. The smooth hysteresis curves signify that both samples have good mechanical stability due to low residual strain and high homogeneity.

Figure 7(c) presents the field-cooled magnetization versus temperature (M–T) curves for the microspheres. Consistent with the M–H results, Sample B2 displays higher magnetization across the entire temperature range measured. Furthermore, a gradual decrease in magnetization with increasing temperature is observed in both samples, resembling the behavior found in magnetically interacting assemblies of magnetite nanostructures [56, 57].

4 Conclusions

Microparticles of iron oxide were fabricated for the first time via the flame method using ferric oxide waste from industrial steel. The fabricated particles exhibit spherical morphology (microspheres, MSs), with an average size distribution of 45 µm (Sample A2) and 60 µm (Sample B2). MSs are mostly composed of magnetite (majority phase) and maghemite phases, which were confirmed using XRD, vibrational (FTIR/Raman) spectroscopy and Mössbauer spectroscopy. MSs presented a very soft ferrimagnetic behavior, with high saturation magnetization, similar to bulk magnetite, and very low remanence and coercivity. This magnetic behavior is required in daily life application such as transformers, memory devices, and motors as they reduce energy loss caused by heating during the continuous reversal of the magnetic field in electrical applications. Overall, this study outlines a pathway for converting waste from the steel industry into eco-friendly materials with promising applications in both industry and environmental contexts.

Acknowledgements This research has been supported by Colombian Government through the projects SGR BPIN 2020000100377 and SGR BPIN 2021000100424, and Universidad del Valle– Colombia (Grant C.I.71342). E. M.-V. thanks Dr. M. Millan-Franco for the discussion on XRD.

Author contributions Conceptualization, E.R., R.A.M.-M., and E.M.-V.; methodology, E.R. and R.A. M.-M.; formal analysis, E.R., L.M., M.M., J.A.T., JL.A.R., J.E.D., and E.M.-V.; investigation, E.R.; resources, E.M.-V.; data curation, R.S. and E.M.-V.; writing—original draft preparation, E.M.-V.; writing—review and editing, R.S. and E.M.-V.; supervision, R.A.M.-M. and E.M.-V.; funding acquisition, E.M.-V. All authors have read and agreed to the published version of the manuscript.

Funding Open Access funding provided by Colombia Consortium. This research was funded by Colombian Government through the projects SGR BPIN 2020000100377.

Data availability Data are contained within the manuscript.

Declarations

Conflict of interest The authors declare that they have no known competing financial interests of personal relationships that could have appeared to influence the work reported in this paper.

References

1. N. Ferroudj, J. Nzimoto, A. Davison, D. Talbot, E. Briot, V. Dupuis, A. Bée, M.S. Medjram, S. Abramson, Maghemite nanoparticles and maghemite/silica nanocomposite microspheres as magnetic Fenton catalysts for the removal of water pollutants. Appl. Catal. B 136–137 (2013). https://doi.org/10.1016/j.apcatb.2013.01.046
2. M.A. Habila, M.S. Moshab, A.M. El-Toni, Z.A. ALOthman, A.Y. Ahmed, B. H. Thermal fabrication of magnetic Fe_3O_4 (nanoparticle)@carbon sheets from waste resourses for the adsorption of dyes: kinetic, equilibrium, and UV-Visible spectroscopy investigations. Nanomaterials. **13**, 1266 (2023). https://doi.org/10.3390/nano13071266
3. E. Rivera, R.A. Muñoz-Meneses, L. Marín, M. Mora, J.E. Tabares, M. Manotas-Albor, L.A. Rodríguez, J.E. Diosa, E. Mosquera-Vargas, Structural, optical and magnetic properties of submicron hematite (α-Fe_2O_3) particles synthesized from industrial steel waste. Mater. Sci. Eng. B **288**, 116170 (2023). https://doi.org/10.1016/j.mseb.2022.116170
4. M.A. Vargas, J.E. Diosa, E. Mosquera, The structural, optical and magnetic property of iron oxides submicron particles synthesized by the pechini method from steel industry wastes. J. Magn. Magn. Mater. **513**, 167243 (2020). https://doi.org/10.1016/j.jmmm.2020.167243
5. J. Balbuena, L. Sánchez, M. Cruz-Yusta, Use of steel industry wastes for the Preparation self-cleaning mortars. Materials. **12**, 621 (2019). https://doi.org/10.3390/ma12040621
6. D.M.S.N. Dissanayake, M.M.M.G.P.G. Mantilaka, T.C. Palihawadana, G.T.D. Chandrakumara, R.T. De Silva, H.M.T.G.A. Pitawala, K.M. de Nalin, G.A.J. Amaratunga, Facile and low-cost synthesis of pure hematite (α-Fe_2O_3) nanoparticles from naturally occurring laterites and their superior adsorption capability towards acid-dyes. RSC Adv. **9**, 21249–21257 (2019). https://doi.org/10.1039/C9RA03756J
7. J. Liu, H. Yang, X. Xue, Preparation of different shaped α-Fe_2O_3 nanoparticles with large particle of iron oxide red. CrystEngComm. **21**, 1097–1101 (2019). https://doi.org/10.1039/C8CE01920G
8. L.M. Cursaru, R.M. Piticescu, D.V. Dragut, I.A. Tudor, V. Kuncser, N. Iacob, F. Stoiciu, The influence of synthesis parameters on structural and magnetic properties of Iron oxide nanomaterials. Nanomaterials. **10**(1), 85 (2020). https://doi.org/10.3390/nano10010085
9. M.A. Vargas, J.E. Diosa, E. Mosquera, Data on study of hematite nanoparticles obtained from Iron(III) oxide by the pechini method. Data Brief. **25**, 104183 (2019). https://doi.org/10.1016/j.dib.2019.104183
10. M. Maruthupandy, T. Muneeswaran, T. Vennila, M. Anand, W.-S. Cho, F. Quero, Development of Chitosan decorated Fe_3O_4 nanospheres for potential enhancement of photocatalytic degradation of congo red dye molecules. Spectrochem Acta A: Mol. Biomol. Spectros. **267**(1), 120511 (2022). https://doi.org/10.1016/j.saa.2021.120511
11. A.S. Teja, P.-Y. Koh, Synthesis, properties, and applications of magnetic iron oxide nanoparticles. Prog Cryst. Growth Charact. Mater. **55**, 22–45 (2009). https://doi.org/10.1016/j.pcrysgrow.2008.08.003
12. J. Hong, F. Yang, Z. Sun, Hexagonal bi-pyramid α-Fe_2O_3 microcrystals: unusual formation, characterization and application for gas sensing. J. Alloys Compd. **889**, 161515 (2022). https://doi.org/10.1016/j.jallcom.2021.161515
13. J.M. Meijer, L. Rossi, Preparation, properties, and applications of magnetic hematite microparticles. Soft Matter. **17**, 2354–2368 (2021). https://doi.org/10.1039/d0sm01977a
14. A.H. Asif, S. Wang, H. Sun, Hematite-based nanomaterials for photocatalytic degradation of pharmaceuticals and personal care products (PPCPs): *A short review*. Curr. Opin. Green. Sustain. Chem. **28**, 100447 (2021). https://doi.org/10.1016/j.cogsc.2021.100447
15. X. He, C. Shang, Q. Meng, Z. Chen, M. Jin, L. Shui, Y. Zhang, Z. Zhang, M. Yuan, X. Wang, K. Kempa, G. Zhou, Hematite photoanode modified with inexpensive hole-storage layer for highly efficient solar water oxidation. Nanotechnology. **31**, 455405 (2020). https://doi.org/10.1088/1361-6528/ab8e74
16. A. Enesca, C. Cazan, Polymer Composite-Based materials with photocatalytic applications in wastewater organic pollutant removal: A Mini review. Polymers. **14**(16), 3291 (2022). https://doi.org/10.3390/polym14163291
17. A. Mirzaei, S.G. Leonardi, G. Neri, Detection of hazardous volatile organic compounds (VOCs) by metal oxide nanostructures-based gas sensors: a review. Ceram. Int. **42**, 15119–15141 (2016). https://doi.org/10.1016/j.ceramint.2016.06.145
18. C. Yu, L. Dongxu, C. Hongyu, Z. Suiyi, W. Xianze, Y. Jiakuan, X. Xinfeng, J. Eskola, B. Dejun, Review of resource utilization of Fe-rich sludges: purification, upcycling, and application in wastewater treatment. Environ. Reviews. **30**, 460–484 (2022). https://doi.org/10.1139/er-2021-0038
19. J. Li, J. You, Z. Wang, Y. Zhao, J. Xu, X. Li, H. Zhang, Application of α-Fe_2O_3-based heterogeneous photo-Fenton catalyst in wastewater treatment: A review of recent advances. J. Environ. Chem. Eng. **10**, 108329 (2022). https://doi.org/10.1016/j.jece.2022.108329
20. G.P. Mastrotheodoros, K.G. Beltsios, Pigments—Iron-based red, yellow, and brown ochres. Archaeol. Anthropol. Sci. **14**, 35 (2022). https://doi.org/10.1007/s12520-021-01482-2
21. N. Murali, S.K. Rainu, N. Singh, S. Betal, Advanced materials and processes for magnetically driven micro- and nano-machines for biomedical application. Biosens. Bioelectron. X. **11**, 100206 (2022). https://doi.org/10.1016/j.biosx.2022.100206
22. L. Lai, Y. He, H. Zhou, B. Huang, G. Yao, B. Lai, Critical review of natural iron-based minerals used as heterogeneous catalysts in peroxide activation processes: characteristics, applications and

mechanisms. J. Hazard. Mater. **416**, 125809 (2021). https://doi.org/10.1016/j.jhazmat.2021.125809
23. K.M.Z. Hossain, U. Patel, I. Ahmed, Development of microspheres for biomedical applications: a review. Pro Biomater. **4**, 1–9 (2015). https://doi.org/10.1007/s40204-014-0033-8
24. J. Molinar Díaz, S.A. Samad, E. Steer, N. Neate, H. Constantin, M.T. Islam, P.D. Brown, Ahmed I. Flame spheroidization of dense and porous $Ca_2Fe_2O_5$ microspheres. Mater. Adv. **1**, 3539 (2020). https://doi.org/10.1039/d0ma00564a
25. M. Knoll, H. Gerhardter, R. Prieler, C. Hochenauer, M. Muhlbock, P. Tomazic, H. Schrottner, Characterization and evaluation of a novel semi-industrial scale vertical shaft furnace for particle spheroidization. J. Energy Inst. **93**, 1110–1124 (2020). https://doi.org/10.1016/j.joei.2019.10.005
26. A. Lassoueda, M.S. Lassoueda, B. Dkhilb, S. Ammara, A. Gadria, Synthesis, structural, morphological, optical and magnetic characterization of iron oxide (α-Fe_2O_3) nanoparticles by precipitation method: effect of varying the nature of precursor. Phys. E Low Dimens Syst. Nanostruct. **97**, 328–334 (2018). https://doi.org/10.1016/j.physe.2017.12.004
27. F. Varret, J. Teillet, M.O.S.F.I.T. Unpublished, program, Maine University, France
28. D.V. de Sousa, J.C. Ker, C.E.R. Schaefer, M.J. Rodet, L.M. Guimaraes, J.F. Felix, Magnetite originating from bonfires in a Brazilian prehistoric anthrosol: a micro-Raman approach. Catena **171**, 552–564 (2018). https://doi.org/10.1016/j.catena.2018.07.036
29. T. Girardet, S. Diliberto, C. Carteret, F. Cleymand, S. Fleutot, Determination of the percentage of magnetite in iron oxide nanoparticles: a comparison between Mössbauer spectroscopy and Raman spectroscopy. Solid State Sci. **143**, 107258 (2023). https://doi.org/10.1016/j.solidstatesciences.2023.107258
30. P.M. Valov, Y.V. Vasilév, G.V. Veriovkin, D.F. Kaplin, Mössbauer spectra of wustite at high temperatures: diffusion line broadening. J. Sol State Chem. **1**, 215–217 (1970). https://doi.org/10.1016/0022-4596(70)90017-4
31. J. Li, J. Wang, J. Li, X. Yang, J. Wan, C. Zheng, Q. Du, G. Zhou, X. Yang, Fabrication of Fe_3O_4@PVA microspheres by one-step electrospray for magnetic resonance imaging during transcatheter arterial embolization. Acta Biomater. **131**, 532–543 (2021). https://doi.org/10.1016/j.actbio.2021.07.006
32. L.H. Maloto, S.S. Manzini, E.D. Dikio, Reduction of magnetite in the presence of activated carbon using mechanical alloying. J. Chem. **2013**, 1–8 (2013). https://doi.org/10.1155/2013/837649
33. O. Ivashchenko, J. Jurga-Stopa, E. Coy, B. Peplinska, Z. Pietralik, S. Jurga, Fourier transform infrared and Raman spectroscopy studies on magnetite/Ag/antibiotic nanocomposites. Appl. Surf. Sci. **364**, 400–409 (2016). https://doi.org/10.1016/j.apsusc.2015.12.149
34. R.D. Waldron, Infrared spectra of ferrite. Phys. Rev. **99**, 1727–1735 (1955)
35. M. Singh, P. Ulbrich, V. Prokopec, P. Svoboda, E. Santava, F. Stepanek, Vapour phase approach for iron oxide nanoparticle synthesis from solid precursors. J. Solid State Chem. **200**, 150–156 (2013). https://doi.org/10.1016/j.jssc.2013.01.037
36. G.A. El-Mahdy, A.M. Atta, H.A. Al-Lohedan, Synthesis and evaluation of poly(sodium 2-acrylamido-2-methylpropane sulfonate-co-styrene)/magnetite nanoparticle composites as corrosion inhibitors for steel. Molecules **19**, 1713–1731 (2014). https://doi.org/10.3390/molecules19021713
37. J. Kraxner, M. Michalek, A. Rincon Romero, H. Elsayed et al., Porous bioactive glass microspheres prepared by f lame synthesis process. Mater. Lett. **256**, 126625 (2019). https://doi.org/10.1016/j.matlet.2019.126625
38. M.G. Verón, E. Rivera Figueroa, M. Prado, O. 45S5 bio-glass flame spheroidization. Chem. Composition Bioactivity Cerâmica. **71**, eRUCJ5814 (2025). https://doi.org/10.1590/RUCJ5814
39. X. Li, Y. Chen, X. Tang, L. Gu, J. Yuan, W. Su, H. Tian, H. Luo, S. Cai, S. Komarneni, Thermally induced phase transition of troilite during micro-Raman spectroscopy analysis. Icarus. **390**, 115299 (2023). https://doi.org/10.1016/j.icarus.2022.115299
40. de D.L.A. Faria, S. Venancio Silva, de M.T. Olivera, Raman microspectrocopy of some iron oxides and oxyhydroxides. J. Raman Spectrosc. **28**, 873–878 (1997). https://doi.org/10.1002/(SICI)1097-4555(199711)28:11/3C873::AID-JRS177/3E3.0.CO;2-B
41. L. Machala, J. Tuček, R. Zbořil, Polymorphous transformations of nanometric iron(III) oxide: A review. Chem. Mater. **23**, 3255 (2011). https://doi.org/10.1021/cm200397g
42. de J.A. Fidelis, R. Pires, M. de Resende, D.S. Costa Lima, G.F. Perdigao, de P.R. Pavia, Da Silva bezerra A. C. Magnetite: properties and applications– A review. J. Mag Mag Mater. **614**, 172770 (2025). https://doi.org/10.1016/j.jmmm.2025.172770
43. H. Shokrollahi, A review of the magnetic properties, synthesis methods and applications of maghemite. J. Mag Mag Mater. **426**, 74–81 (2017). https://doi.org/10.1016/j.jmmm.2016.11.033
44. M.D. Nguyen, H.-V. Tran, S. Xu, T.R. Lee, Fe_3O_4 nanoparticles: structures, synthesis, magnetic properties, surface functionalization, and emerging applications. Appl. Sci. **11**, 11301 (2021). https://doi.org/10.3390/app112311301
45. M. Chirita, A. Bezergheanu, C. Bazil Cizmas, A. Ercuta, Superparamagnetic-like micrometric single crystalline magnetite for biomedical application synthesis and characterization. Magnetochemistry. **9**, 5 (2023). https://doi.org/10.3390/magnetochemistry9010005
46. A. Sabur, A. Gafur, Crystallographic, Morphological, Magnetic, and Thermal Characterization of Superparamagnetic Magnetite Nanoparticles (Fe_3O_4) Synthesized by Chemical Coprecipitation Method and Calcined at 250°C for 4 hr. J. Nanomater. **9577778**, 9 (2024). https://doi.org/10.1155/2024/9577778
47. A. Akbar, S. Riaz, M. Bashir, S. Naseem, Effect of Fe^{3+}/Fe^{2+} ratio on superparamagnetic behavior of spin coated iron oxide thin films. IEEE Trans. Magn. **50**(8), 2200804 (2014). https://doi.org/10.1109/TMAG.2014.2312972
48. D.H. Ha, J.P. Wang, H.L. Luo, Crystallite size effect on saturation magnetization of fine ferrimagnetic particles. J. Mag Mag Mater. **136**, 176–182 (1994). https://doi.org/10.1016/0304-8853(94)90462-6
49. S. Upadhayay, K. Parekh, B. Pandey, Influence of crystallite size on the magnetic properties of Fe_3O_4 nanoparticles. J. Alloys Comp. **678**, 478–485 (2016). https://doi.org/10.1016/j.jallcom.2016.03.279
50. N. Saxena, M. Singh, Efficient synthesis of superparamagnetic magnetite nanoparticles under air for biomedical applications. J. Mag. Mag. Mater. **429**, 166–176 (2017). https://doi.org/10.1016/j.jmmm.2017.01.031
51. N. Sezer, I. Ari, Y. Biçer, M. Koç, Superparamagnetic nanoarchitectures: multimodal functionalities and applications. J. Mag Mag Mater. **538**, 168300 (2021). https://doi.org/10.1016/j.jmmm.2021.168300
52. V. Reichel, A. Kovács, M. Kumari et al., Single crystalline superstructured stable single domain magnetite nanoparticles. Sci. Rep. **7**, 45484 (2017). https://doi.org/10.1038/srep45484
53. Y. Zhang, M. Liu, Y. Zhang, X. Chen, W. Ren, Ye Z.-G. Atomic layer deposition of superparamagnetic and ferrimagnetic magnetite thin films. J. Appl. Phys. **115**, 17C743 (2015). https://doi.org/10.1063/1.4916818
54. N.I. Cuello, E.G. Fornasin, M.I. Oliva, G.F. Goya, G. Marchetti, G.A. Eimer, V.R. Elías, Maghemite and hematite nanowires synthesized by nanocasting: precursor effects on structural and

magnetic properties. J. Mag Mag Mater. **629**, 173288 (2025). https://doi.org/10.1016/j.jmmm.2025.173288

55. X.H. Liu, W. Liu, Z.D. Zhang, Extremely low coercivity in Fe3O4 thin film grown on Mg2TiO4 (001). RSC Adv. **7**, 43648–43654 (2017). https://doi.org/10.1039/C7RA08916C
56. Y.A. Urian, J.J. Atoche-Medrano, L.T. Quispe, F.L. León, J.A. Coaquira, H. Study of the surface properties and particle-particle interactions in oleic acid-coated Fe_3O_4 nanoparticles. J. Mag Mag Mater. **525**, 167686 (2021). https://doi.org/10.1016/j.jmmm.2020.167686
57. D.A. Balaev, S.V. Semenov, A.A. Dubrovskiy, S.S. Yakushkin, V.L. Kirillov, O. Martyanov, N. Superparamagnetic blocking of an ensemble of magnetite nanoparticles upon interparticle interactions. J. Mag Mag Mater. **440**, 199–202 (2017). https://doi.org/10.1016/j.jmmm.2016.12.046